Geophysical Journal International

Geophys. J. Int. (2020) **220,** 1804–1812
Advance Access publication 2019 December 6
GJI General Geophysical Methods

doi: 10.1093/gji/ggz556

A solid/fluid substitution scheme constrained by pore-scale numerical simulations

Yongyang Sun,[1] Boris Gurevich,[1,2] Stanislav Glubokovskikh,[1] Maxim Lebedev,[1]
Andrew Squelch,[1] Christoph Arns[3] and Junxin Guo[4,5]

[1] *Department of Exploration Geophysics, Curtin University, GPO Box U*1987*, Perth, WA* 6845*, Australia. E-mail:* yongyang.sun@postgrad.curtin.edu.au
[2] *CSIRO,* 26 *Dick Perry Avenue, Kensington, WA* 6151*, Australia*
[3] *University of New South Wales, Sydney, NSW* 2052*, Australia*
[4] *Department of Earth and Space Sciences, Southern University of Science and Technology, Shenzhen* 518055*, China*
[5] *School of Earth and Space Sciences, University of Science and Technology of China, Hefei* 230026*, China*

Accepted 2019 November 26. Received 2019 November 26; in original form 2019 August 27

SUMMARY

Estimating the effects of pore filling material on the elastic moduli or velocities of porous and fractured rocks attracts widespread attention. This effect can be modelled by a recently proposed triple-porosity scheme, which quantifies this effect from parameters of the pressure dependency of the elastic properties of the dry rock. This scheme divides total porosity into three parts: compliant, intermediate and stiff. Each type of pores is assumed to be spheroidal and characterized by a single aspect ratio. However, the implementation of this model requires the asymptotic values of the elastic moduli at much higher pressures where only non-closable pores remain open. Those pressures are beyond the capacity of most rock physics laboratories and can even crush typical sandstone samples. Experimental data at such pressures are usually unavailable. To address this issue, we introduce pore-scale numerical simulations in conjunction with effective medium theories (EMT) to compute the asymptotic values directly from the microtomographic images. This workflow reduces the uncertainty of model predictions on the geometric information of stiff pores and strengthens the predictive power and usefulness of the model without any adjustable parameters. Applying this to a Bentheim sandstone fully filled with liquid and solid octadecane gives a reasonable match between model predictions and laboratory measurements. This success verifies the accuracy and applicability of the model and indicates its potential in further exploitation and characterization of heavy oil reservoirs and other similar reservoirs.

Key words: Acoustic properties; Seismic attenuation; Microstructure.

1 INTRODUCTION

A link between the elastic moduli of rocks and the properties of pore-filling materials is required for many geophysical applications such as reservoir characterization from seismic data or 4-D seismic monitoring. Establishing such a link requires an understanding of the interactions among the rock matrix, pore space, and solid or liquid pore fill. Pore fill can be gas (e.g. air, hydrocarbon gas, CO_2 and steam), liquid (e.g. brine, oil, magma) or solid (e.g. kerogen, bitumen, salt, ice, gas hydrates, etc.) (Saxena *et al.* 2016). For a fluid pore fill (liquid or gas), the Gassmann (1951) equation gives an exact relationship between the dry and saturated moduli, and has been widely employed to predict the change in saturated elastic moduli upon the change of fluid properties without any detailed geometrics information (Smith *et al.* 2003). The Gassmann theory also stipulates that the effective shear modulus is unaffected by the pore fluid properties (Berryman 1999). However, the Gassmann theory has an important restriction: it assumes that the pressure in the pore fill is spatially uniform. Thus for rocks filled with solid substances or high-viscosity or non-Newtonian fluids, the Gassmann theory is invalid as the shear compliance of the pore fill impedes the pressure communication between different pores (Makarynska *et al.* 2010; Saxena & Mavko 2014; Glubokovskikh *et al.* 2016; Sun *et al.* 2018).

Ciz & Shapiro (2007, referred to as C&S model) derived an approximate extension of the Gassmann equation to a solid pore fill. However, recent studies (Saxena & Mavko 2014; Glubokovskikh *et al.* 2016; Sun *et al.* 2018) show that the C&S model gives a lower bound to the elastic moduli of porous and fractured rocks saturated with a solid or high-viscosity liquid because it also assumes that stress throughout the pore fill is spatially uniform. This assumption should be accurate if all pores are of approximately the same shape, but can be violated if the pore space contains pores with a range of shapes and compliances.

Laboratory experiments show that the dry moduli increase with increasing effective pressure (which is defined as the difference between the confining pressure and pore pressure). Several authors have ascribed the significant initial change in elastic moduli with increasing effective pressure to the closure of crack-like compliant pores (Walsh 1965; Zimmerman *et al.* 1986; Shapiro 2003). In particular, Shapiro (2003) developed a model based on a binary pore structure by dividing the total porosity into two parts: stiff or equant porosity, which is the dominant portion of the pore space, and soft or compliant porosity, whose total volume is small, but which controls the pressure dependency of the elastic moduli. Makarynska *et al.* (2010) showed that the presence of compliant pores increases the effect of the solid pore fill on the effective moduli—an effect similar to squirt flow in rocks saturated with a fluid at ultrasonic frequencies (see Leurer & Dvorkin 2006).

The disproportional effect of the compliant pores on the elastic moduli of rocks saturated with a solid is modelled by Saxena & Mavko (2015). However, their approach assumes that the compliant pores are isolated from the stiff pores. Therefore, the stress in the pore fill is not uniform and hence the scheme of Saxena & Mavko (2015) does not reduce to the Gassmann equation for a fluid pore fill. To ensure Gassmann consistency, Glubokovskikh *et al.* (2016) modelled the compliant pores as grain-to-grain contacts open into stiff pores. Compliant pores are modelled as thin circular disks with traction-free edges. The stiffness of the disk is calculated using the solution of the elastic problem by Tsai & Lee (1998). Although this model gives the general trend of the overall elastic moduli resulting from the solid pore fill, the model predictions systematically deviate from experimental data, especially for the shear modulus. This discrepancy is similar to the one observed for liquid-filled rocks at ultrasonic frequencies (de Paula *et al.* 2012) and probably occurred because the binary structure model of the pore space is oversimplified. Indeed some studies show that in addition to compliant and stiff pores there exist pores with intermediate compliance, which are responsible for gradual increase of the dry bulk and shear moduli with pressure of up to hundreds of MPa (Shapiro 2003; Wang *et al.* 2005; Adelinet *et al.* 2010).

Recently, Sun *et al.* (2018) generalized the model of Glubokovskikh *et al.* (2016) to a triple-porosity scheme by adding, similarly to de Paula *et al.* (2012), a newly defined type of pores called intermediate pores. Intermediate pores are defined as having an aspect ratio between that of compliant pores and of the stiff pores. The pressure dependency of the dry moduli is governed by the conjunction of those three pore structures. Two kinds of stress relaxation within the pore space are modelled: (1) between compliant and 'stiff' (plus intermediate pores) pores in a relatively low pressure range and (2) between intermediate and stiff pores in a high pressure range. Intermediate porosity decreases in an exponential way at much higher pressures, which behaves similar to the compliant porosity at lower pressures. However, the implementation of this method requires the dry bulk and shear moduli K_{hm} and μ_{hm} in high-pressure limit where rocks are assumed to contain stiff pores only. The pressures corresponding to this limit (200−500 MPa) are beyond the capacity of most rock physics laboratories and can even crush typical sandstone samples (Zhang *et al.* 1990; Wong *et al.* 1997; Fortin *et al.* 2007). Therefore, K_{hm} and μ_{hm} cannot be measured directly. Sun *et al.* (2018) computed K_{hm} and μ_{hm} using an effective medium theory (EMT). This approach requires knowledge of the aspect ratio of stiff pores. Detailed analysis of this issue gives a plausible range of such aspect ratios, and thus the model predicts a range of the elastic moduli of solid-filled sandstone. Sun *et al.* (2018) applied this approach to a Bentheim sandstone fully saturated with solid octadecane and found that the experimental data lie well within the predicted range. Yet, the prediction uncertainty (associated with lack of knowledge of the effective aspect ratio of stiff pores) reduces the predictive power and usefulness of the theoretical model.

The aim of this paper is to eliminate the uncertainty of model predictions by determining the effective aspect ratio of stiff pores directly from microtomographic images of the pore samples. This is done by numerically simulating K_{hm} and μ_{hm} directly from the 3-D image of a rock fragment using finite element method (FEM) (Roberts & Garboczi 2000; Arns *et al.* 2001, 2002), and inverting these moduli for the aspect ratio using the EMT (assuming that most of the porosity resolved in the image is stiff porosity). An alternative would be to use simulated K_{hm} and μ_{hm} directly in the theoretical model. However, such moduli would likely vary from fragment to fragment due to spatial variation of porosity. Determining the effective aspect ratio of stiff pores is likely to be more robust.

In this work, we first reproduce the theories of the triple-porosity model and modify the workflow by pore-scale numerical simulations based on FEM. We then demonstrate the details of how numerical simulations help constrain the predictions of the triple-porosity model. In the end, we compare the modified model predictions with other solid substitutions schemes against the laboratory measurements.

2 TRIPLE-POROSITY MODEL

In order to account for the pressure dependency of the elastic moduli, Sun *et al.* (2018) proposed a triple-porosity model, in which the pore space is divided into stiff, intermediate and compliant pores. This triple-porosity structure is necessary for adequate characterization of the pore geometry, which in turn is essential for modelling the fluid effects (de Paula *et al.* 2012; Sun *et al.* 2018). Total porosity ϕ is divided into three parts: compliant ϕ_c, intermediate ϕ_m and stiff ϕ_s. The three types of pores are modelled as spheroids, each with a different aspect ratio. The main results that are used to compute the 'unrelaxed' frame moduli K_{uf} and μ_{uf}, which correspond to the moduli of a hypothetical rock in which all non-stiff pores (including compliant and intermediate pores in this work) are fully saturated with fluid and stiff pores remain empty, are described by the following equations (Sun *et al.* 2018):

$$\frac{1}{K_{uf}} = \frac{1}{K_{hm}} + \frac{1}{\dfrac{1}{\dfrac{1}{K_{dry}} - \dfrac{1}{K_d}} + \dfrac{M_{fc}}{\phi_c}} + \frac{1}{\dfrac{1}{\dfrac{1}{K_d} - \dfrac{1}{K_{hm}}} + \dfrac{M_{fm}}{\phi_m}} \tag{1}$$

and

$$\frac{1}{\mu_{uf}} = \frac{1}{\mu_{hm}} + \frac{4}{15}\left(\frac{1}{K_{uf}} - \frac{1}{K_d}\right) + \frac{1}{\dfrac{1}{\dfrac{1}{\mu_{dry}} - \dfrac{1}{\mu_d} - \dfrac{4}{15}\left(\dfrac{1}{K_{dry}} - \dfrac{1}{K_d}\right)} + \dfrac{5}{2}\dfrac{\mu_f}{\phi_c}} + \frac{1}{\dfrac{1}{\dfrac{1}{\mu_d} - \dfrac{1}{\mu_{hm}} - \dfrac{4}{15}\left(\dfrac{1}{K_d} - \dfrac{1}{K_{hm}}\right)} + \dfrac{5}{2}\dfrac{\mu_f}{\phi_m}}, \tag{2}$$

where K_{hm} and μ_{hm} are the high-pressure dry moduli (in this high-pressure limit all pores except stiff pores are assumed completely closed), K_{dry} and μ_{dry} are the pressure-dependent dry moduli calculated directly from ultrasonic velocities and density, K_d and μ_d correspond to the dry moduli of a hypothetical rock in which compliant pores are closed, ϕ_c and ϕ_m are the pressure-dependent compliant and intermediate porosity, respectively, μ_f is the shear modulus of the pore fill, and M_{fc} and M_{fm} are the modified compression stiffness of a typical fluid- or solid-saturated compliant and intermediate pore respectively as given by Tsai & Lee (1998).

Once K_{uf} and μ_{uf} are obtained, we can compute the undrained moduli by saturating the remaining stiff porosity using the lower embedded bound theory (Mavko & Saxena 2013; Saxena & Mavko 2014; Glubokovskikh *et al.* 2016). We do not reproduce the derivation details but outline the workflow to obtain all the parameters (K_{hm}, μ_{hm}, ϕ_c, ϕ_m, K_d, μ_d, M_{fc} and M_{fm}) in equations (1) and (2) (an extension of the workflow described by Sun *et al.* (2018).

(1) Dry moduli K_{dry} and μ_{dry} are computed from the pressure dependency of ultrasonic *P*- and *S*-wave velocities and the measured density.

(2) Parameters of compliant pores (ϕ_{c0},θ_c, α_c) are obtained directly from the deformation equations (3) and (4) based on the dual-porosity model by Shapiro (2003) through the least square fitting of the pressure dependency of the dry moduli calculated in step (1).

$$K_{dry} = K_{hc}\left[1 + \theta_s\left(\frac{1}{K_{hc}} - \frac{1}{K_g}\right)P - \theta_c\phi_{c0}e^{-\frac{\theta_c P}{K_{hc}}}\right] \tag{3}$$

and

$$\mu_{dry} = \mu_{hc}\left[1 + \theta_{s\mu}\left(\frac{1}{\mu_{hc}} - \frac{1}{\mu_g}\right)P - \theta_{c\mu}\phi_{c0}e^{-\frac{\theta_c P}{K_{hc}}}\right], \tag{4}$$

where K_{hc} and μ_{hc} represent the dry moduli of a hypothetical rock in which compliant pores are closed and the porosity of stiff pores equal to zero-pressure value, ϕ_{c0} is the initial compliant porosity at zero pressure, K_g and μ_g are the bulk and shear moduli of the mineral matrix, θ_c and $\theta_{c\mu}$ are the bulk and shear stress sensitivity coefficients of compliant pores, and θ_s and $\theta_{s\mu}$ are the bulk and shear stress sensitivity coefficients of stiff pores.

(3) Similarly to compliant pores, parameters of intermediate pores (K_{hm}, μ_{hm}, ϕ_{m0}, θ_m, $\theta_{\mu m}$) could be derived directly from the deformation equations

$$K_d = K_{hm}\left[1 - \theta_m\phi_{m0}e^{-\frac{\theta_m P}{K_{hm}}}\right] \tag{5}$$

and

$$\mu_d = \mu_{hm}\left[1 - \theta_{\mu m}\phi_{m0}e^{-\frac{\theta_m P}{K_{hm}}}\right], \tag{6}$$

where θ_m and $\theta_{\mu m}$ are the bulk and shear stress sensitivity coefficients of intermediate pores. ϕ_{m0} is the initial intermediate porosity at zero pressure. For large pressures where compliant pores are closed, $K_d = K_{dry}$ and $\mu_d = \mu_{dry}$. K_d can be obtained from the sum of K_{dry} and the exponential term $K_{\mathrm{hc}}\theta_c\phi_{c0}e^{-\frac{\theta_c P}{K_{hc}}}$, and μ_d can be obtained in the same way. If the pressure dependencies of the dry moduli are available at relatively high pressures (50−500 MPa), the parameters (K_{hm}, μ_{hm}, ϕ_{m0}, θ_m, $\theta_{\mu m}$) can be obtained by the least-square fitting directly. However, ultrasonic velocities at these pressures are seldom available. Thus, we choose to compute the elastic moduli K_{hm} and μ_{hm} by pore-scale numerical simulations using finite element method. At the voxel size of 2−5 μm these images do not contain compliant or even intermediate pores, and thus the simulated dry moduli can be expected to correspond to the moduli of the rock containing only stiff pores (so called ‘Swiss Cheese’ rock, see Shapiro 2003). This assumption is consistent with the results of Saenger *et al.* (2016), who simulated elastic properties from digital images obtained under different confining pressures and found that simulated *P*- and *S*-wave velocities are not sensitive to the confining pressure. Then, other parameters (ϕ_{m0}, θ_m, $\theta_{\mu m}$) of intermediate pores can be obtained from K_{hm} and μ_{hm}, as well as from the slope of the linear decay of the intermediate porosity versus pressure at relatively small effective pressures. This slope is in turn obtained from the first-order Taylor expansion (7) and (8) of deformation equations (5) and (6)

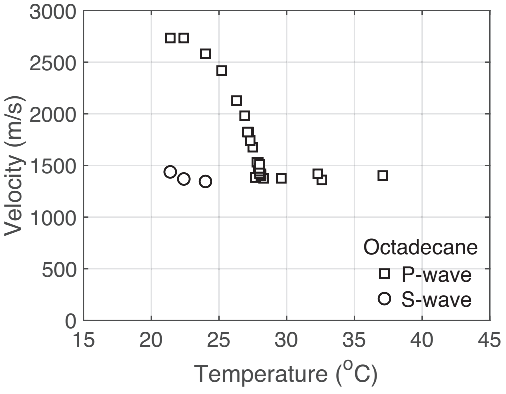

Figure 1. Ultrasonic *P*- (open squares) and *S*-wave (open circles) velocities of octadecane as a function of temperature.

$$K_d = K_{hm}\ (1 - \theta_m\phi_{m0}) + \theta_m^2\phi_{m0}P \tag{7}$$

and

$$\mu_d = \mu_{hm}\left(1 - \theta_{\mu m}\phi_{m0} + \frac{\theta_{\mu m}\theta_m\phi_{m0}}{K_{hm}}\right). \tag{8}$$

(4) Pore-scale numerical simulations can only be performed on a pore-scale image of a mm-size rock fragment. Since porosity can be spatially varying, the simulation results depend on the choice of the fragment, which in turn creates an uncertainty in K_{hm} and μ_{hm}. To deal with this issue, we choose to invert the effective aspect ratio of stiff pores using the EMT based on the numerical simulation. We then substitute the obtained aspect ratio and measured total porosity of the entire sample into the same EMT to calculate K_{hm} and μ_{hm}.

(5) With all the parameters obtained from previous steps, we then calculate the unrelaxed rock frame moduli using equations (1) and (2).

(6) Finally, we compute the fully saturated moduli through the lower embedded bound theory by saturating the remaining open stiff pores with a fluid or a true solid.

Previous workflow presents the procedure of using the triple-porosity scheme to estimate the effective moduli of porous rocks saturated with fluids or true solids. Within the workflow, pore-scale numerical simulations are key in deriving the parameters of intermediate pores and are described in next section.

3 APPLICATION

3.1 Experimental data of a Bentheim sandstone

In order to illustrate the validity and applicability of the modified model constrained by pore-scale numerical simulation presented in previous sections, we apply the model to the data of Sun *et al.* (2018). This ultrasonic data is measured on a Bentheim sandstone,

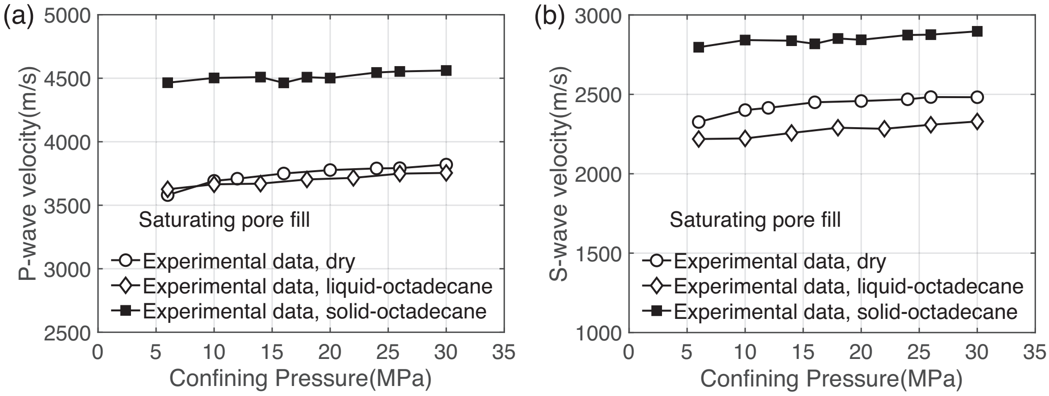

Figure 2. Ultrasonic *P* wave (a) and *S* wave (b) of the dry (open circles), liquid- (open squares) and solid-octadecane-saturated (solid squares) Bentheim sandstone as a function of confining pressures.

Table 1. Material properties for the mineral (Vernik 1998) and pore fills used for the modeling and simulations. K_g and μ_g is the bulk and shear moduli of matrix.

K_g	μ_g	K_f (solid)	μ_f (solid)	K_f (fluid)	ϕ
37.3 GPa	38.2 GPa	3.87 GPa	1.46 GPa	1.53 GPa	23.56 per cent

which has a porosity of 23.56 per cent and is very homogeneous, predominantly comprised of 97 per cent quartz with small portion of accessory feldspars, heavy minerals and Fe-(hydr) oxides (Dubelaar & Nijland 2015). As shown in Fig. 1, the pore fill, octadecane, was chosen because it has a melting/freezing point of $T_{\mathrm{m}} = 28$ °C, making it easy to perform laboratory experiments with this substance in both liquid and solid states.

Figs 2(a) and (b) demonstrate the laboratory measurements of ultrasonic *P*- and *S*-wave velocities of the sample in a dry state (open circles) and liquid- (open diamonds) and solid-octadecane (solid squares) saturated in the pressure range of 6–30 MPa. In the dry state, both *P*- and *S*-wave velocities increase clearly with the increasing confining pressure. However, under the condition of solid-octadecane saturated, the pressure dependency of velocities is reduced. To model this difference, we will need the physical properties of the dry sample and octadecane in liquid and solid forms. These properties are summarized in Table 1.

Note that the ultrasonic measurements on dry sample yield the dry bulk and shear moduli of the rock as the dry velocities are not dispersive (Adelinet *et al.* 2010; Adam & Otheim 2013). Hence, the dry moduli can be obtained directly from those dry velocities and measured density. In the following sections, we will present analysis of velocities and moduli as functions of confining pressure rather than effective pressure, because it is impossible to independently control pore pressure in the solid pore fill.

3.2 Numerical simulations

3.2.1 Image acquisition

Digital rock images used in this study are acquired by 3-D X-ray microscope VeraXRM-500 (ZRadia-Zeiss) at X-ray energy of 60 kV at the voxel size of 2 μm on the same Bentheim sandstone For simulation purposes, image segmentation—which is the procedure of attributing different ranges of grey levels to various phases—controls the accuracy of pore-scale numerical simulations. The first step in this procedure is using a 3-D non-local filter to supress the noise effects. The threshold image segmentation is achieved using combination of Avizo 9.3 software (mainly image processing) and the ImageJ/Fiji software with the 3-D ImageJ Suite plugin (analysis, Ollion *et al.* 2013). The maximum size of the original data set obtained from the cylindrical core samples is 510 × 550 × 893 voxels. As shown in Figs 3(a)–(d), several subsets of different sizes, are extracted for numerical simulations. All these subsets have the same voxel size of 2 μm and are segmented to two-phase images: mineral matrix and pore space.

3.2.2 Property prediction

Microstructures defined by the extracted digital images have been already discretized and ready for the numerical computation of elastic moduli. We calculate the elastic moduli of the mixture system with FEM (Roberts & Garboczi 2000; Arns *et al.* 2001, 2002). The digital image is assumed to have periodic boundary conditions. Elastic moduli of the matrix are set to $K_g = 37.3$ GPa and $\mu_g = 38.3$ GPa, given by Vernik (1998) (average values of the elastic moduli of clean arenites and arenites). Elastic moduli of the pore fill K_f and μ_f are set to zero in order to simulate the dry moduli. Numerical simulation results based on the four different discretized images (Figs 3a–d) are presented in Table 2.

Table 2 shows that all the simulations overestimate the dry elastic moduli compared with the experimental data at pressure $P_e = 6$ MPa. This is consistent with the previous assumption that numerical simulations from microtomographic X-ray images only corresponds to the effects of stiff pores. We assume that the 'best' simulation results are identical to the high-pressure limit moduli K_{hm} and μ_{hm}. This cannot be established directly. Indeed, not only laboratory equipment is mostly limited to $P < 50$–100 MPa, but even if we could measure rocks at pressures of 200–2000 MPa, these pressures would likely be outside the elastic regime. However, as suggested by a number of authors (Arns *et al.* 2007; Andrä *et al.* 2013; Saenger *et al.* 2016), we can infer this information indirectly. A typical X-ray microtomographic has a linear size of 1000 voxels and is about 10−50 average linear sand grain sizes. Thus, a typical grain has a length of about 20−100 voxels. The thinnest grain contacts that can be confidently resolved have a thickness of 5 voxels (at least!). Hence the smallest aspect ratio that can be resolved is $a = 0.05$–0.25 (or larger if we need more. These contacts will close at pressures $P = aK$, where K is bulk modulus of the rock matrix. For the Bentheim sandstone, $K \sim 10$ GPa; this gives P on the order of 500−2500 MPa. However, the simulations presented in Table 2 show that numerical simulations depend on the choice of

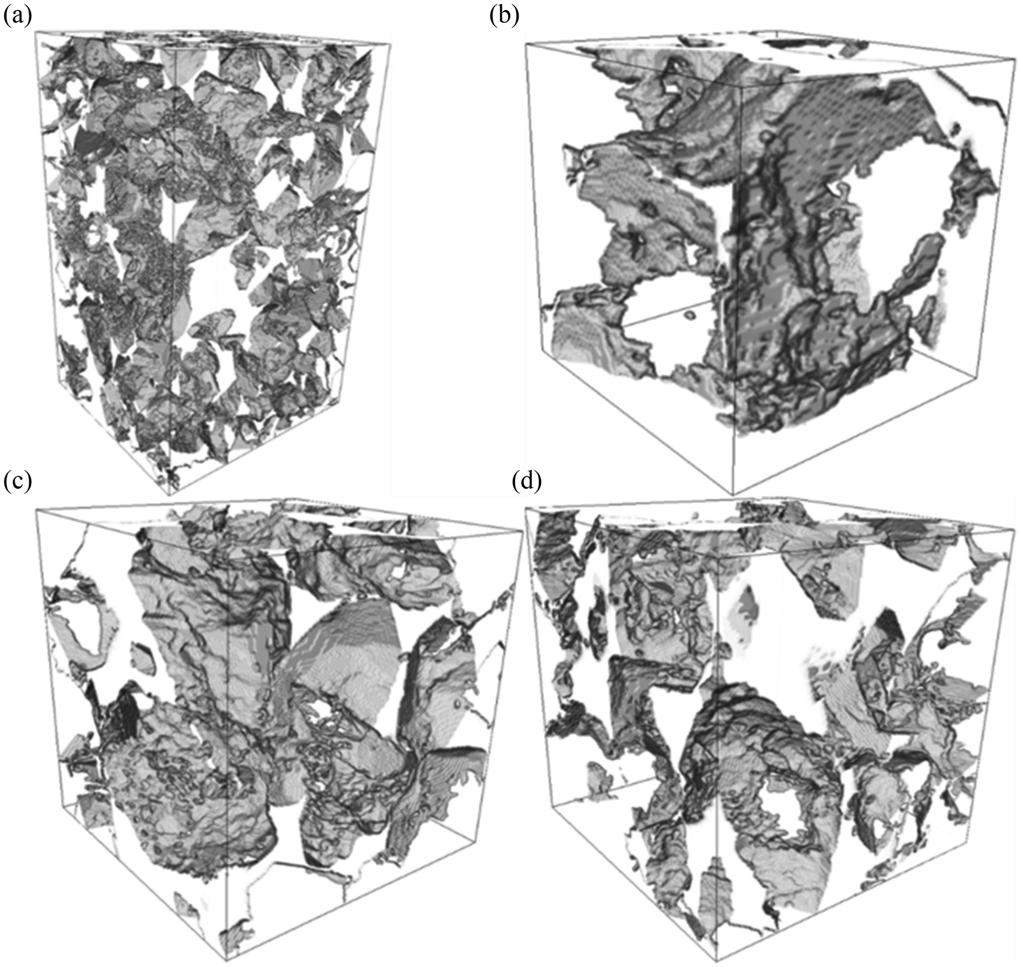

Figure 3. Pore space images of different sizes (a) 510 × 550 × 893, (b) 128 × 128 × 128, (c) 256 × 256 × 256, and (d) 256 × 256 × 256 of subsets extracted from the original cylinder core plugs with the same voxel size of 2 μm. Images (c) and (d) are the subsets of the same size extracted from different place in the original data set.

Table 2. Simulated dry moduli using different fragments of the digital images.

	K_{dry} (GPa)	μ_{dry} (GPa)	ϕ
128 × 128 × 128	19.06	18.49	18.65 per cent
256 × 256 × 256 (upper)	15.98	14.17	21.73 per cent
256 × 256 × 256 (lower)	13.76	13.20	25.84 per cent
510 × 550 × 893	17.06	16.29	21.34 per cent
$P_e = 6$ MPa	11.67	9.59	

the fragment, which in turn creates an uncertainty in K_{hm} and μ_{hm}. To address this issue, we use the simulation results in conjunction with EMT to determine the effective aspect ratio of stiff pores and then substitute the aspect ratio into the same EMT to compute K_{hm} and μ_{hm}.

3.2.3 Computation of the aspect ratio of stiff pores

In order to compute the aspect ratio of stiff pores, in Figs 4(a) and (b), we compare the numerical simulation results (open circles) against the predictions given by the Self-Consistent Approximation (SCA, Berryman 1980; Ogushwitz 1985) method, assuming the pore geometry of spheres (red dashed line), needles (blue dotted line), and spheroids with an aspect ratio of 0.5 (dashed line), 0.23 (solid line) and 0.1 (dotted line). We note that the predictions given by setting the aspect ratio of stiff pores to 0.23 provide a satisfactory fit to our numerical simulation results. Then, in Figs 5(a) and (b), we compare the numerical simulation results against the predictions given by different EMT methods: the SCA, Kuster-Toksoz (referred to as KT) model (Kuster & Toksöz 1974) and differential effective medium theory (referred to as DEM, Cleary *et al.* 1980; Norris 1985; Zimmerman 1991) using the same aspect ratio of 0.23 for stiff pores. The SCA method gives the predictions closest to our numerical predictions. This suggests that the SCA method is the best option to compute the effective aspect ratio of stiff pores.

We then compute the high-pressure limit moduli K_{hm} = 14.74 GPa and μ_{hm} = 14.20 GPa by substituting the aspect ratio of stiff pores $\alpha_s = 0.23$ into the SCA method. Then, following the eqs (7) and (8) in the previous section, we obtain the parameters of intermediate pores (θ_m, $\theta_{\mu m}$, ϕ_{m0}). To this end, as shown in Table 3, all the parameters required in the eqs (1) and (2) are obtained from the pressure dependency of ultrasonic velocities and density. We then compare the model predictions against the experimental data in next section.

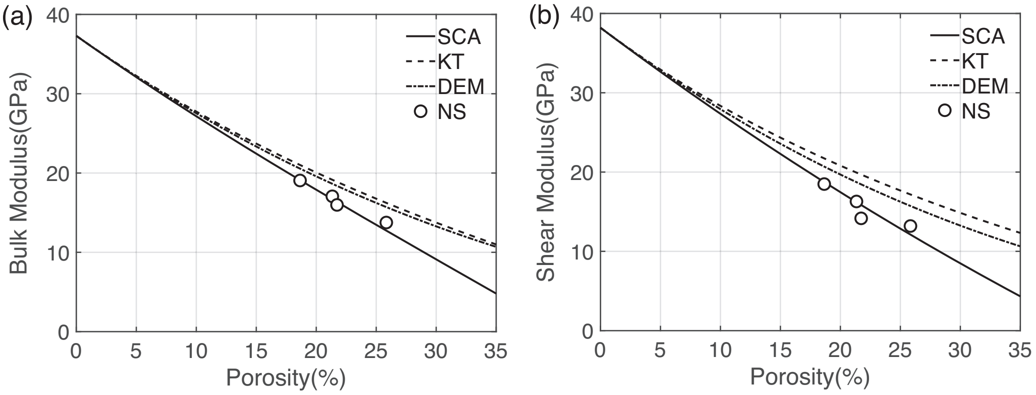

Figure 4. Comparison of the pore-scale numerical simulations to the predictions for the dry bulk (a) and shear (b) moduli using the SCA method assuming different pore shapes.

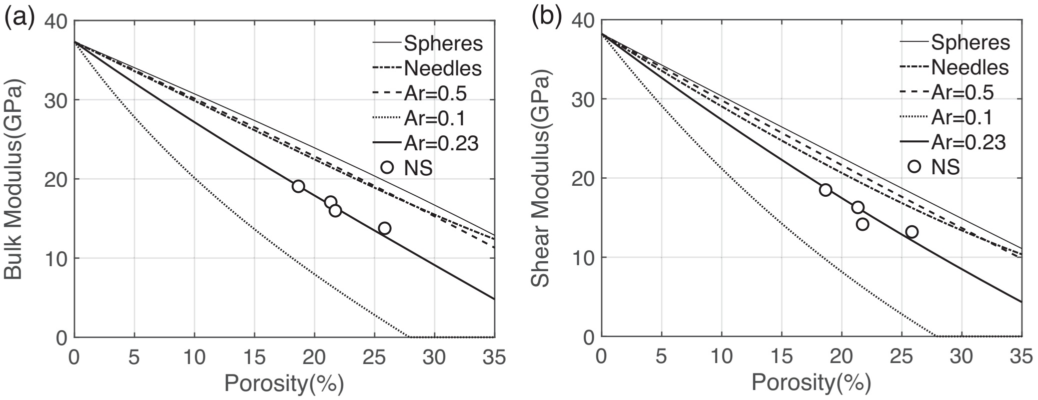

Figure 5. Comparison of the pore-scale numerical simulations to a range of theories used to predict the dry bulk (a) and shear (b) moduli using the same aspect ratio of 0.23 for stiff pores.

Table 3. The parameters of compliant and intermediate porosity of the Bentheimer sandstone obtained by applying the workflow of Section 3 to ultrasonic measurements in a dry state.

θ_c	α_c	θ_m	α_m	ϕ_{c0}	ϕ_{m0}
3.16×10^3	1.78×10^{-4}	1.37×10^2	4.2×10^{-3}	9.75×10^{-4}	1.6×10^{-3}

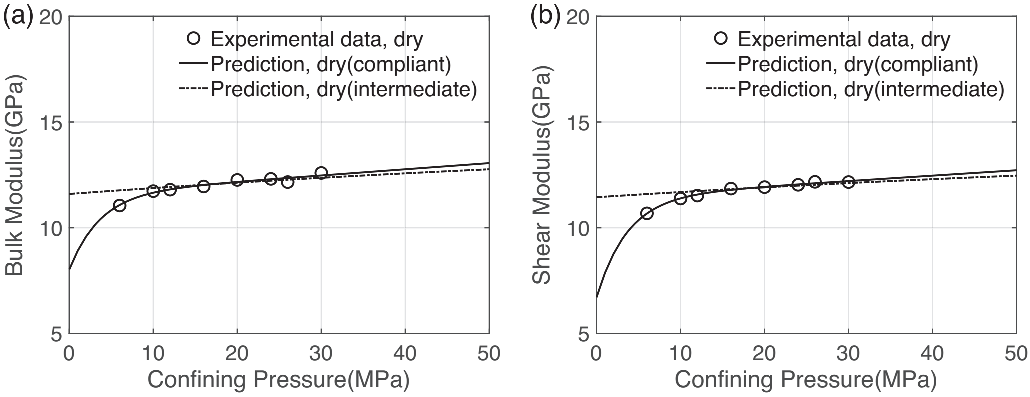

Figure 6. Dry bulk (a) and shear (b) moduli of a Bentheim sandstone as a function of pressure up to 50 MPa. The bulk and shear moduli calculated from the ultrasonic velocities are shown by open circles. Variations of the elastic moduli modelled for low pressures and caused by the closure of the compliant and intermediate pores are shown by the solid line and dashed–dotted line, respectively.

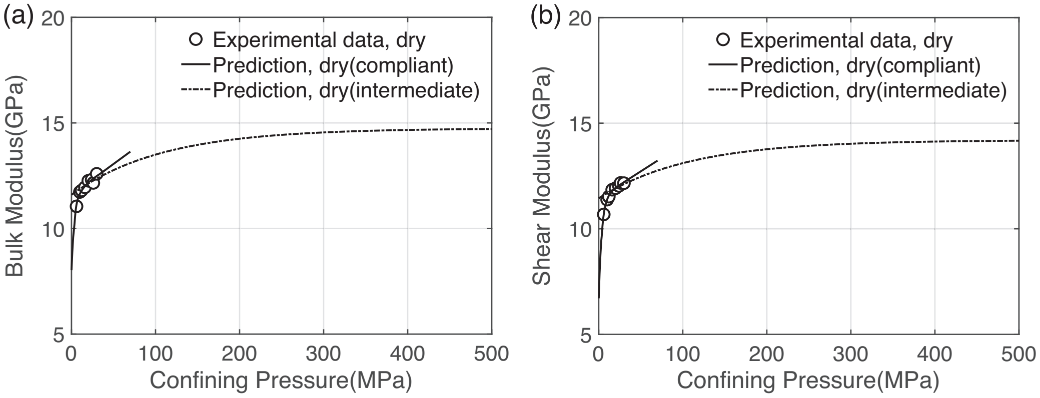

Figure 7. Dry bulk (a) and shear (b) moduli of a Bentheim sandstone as a function of pressure up to 500 MPa. The bulk and shear moduli calculated from the ultrasonic velocities are shown by open circles. Variations of the elastic moduli modelled for low pressures and caused by the closure of the compliant and intermediate pores are shown by the solid line and dashed–dotted line, respectively.

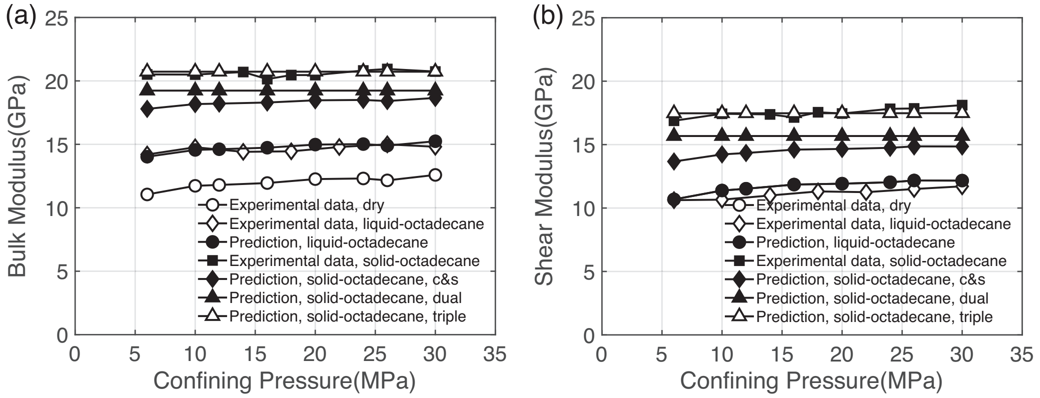

Figure 8. Comparison of the experimental bulk (a) and shear (b) moduli of a Bentheim sandstone saturated with liquid- and solid-octadecane against predictions of different models as a function of confining pressure. Open circles, diamonds and solid squares are the dry, liquid- and solid-octadecane-saturated moduli calculated from the ultrasonic velocities and density respectively. Open triangles are the predictions of the triple-porosity scheme constrained by pore-scale numerical simulations. Solid diamonds and triangles are the predictions of the C&S and dual-porosity models.

Alternatively, aspect ratio could be estimated by inverting the moduli of each fragment (Arns *et al.* 2003; Liu *et al.* 2018). Given that the moduli for all fragments closely follow the single aspect ratio trend (Figs 4 and 5), this approach should give similar results.

3.3 Results

Figs 6(a) and (b) show the least square fitting of the theoretical pressure dependency of the dry moduli (solid line) to the measurements (open circles) for pressures up to 50 MPa. We observe that a combination of exponential and linear terms accounts well for the increase of the dry moduli with the increasing effective pressure. Note that the exponential trend attributed to the compliant cracks closure vanishes within 10−20 MPa. On the other hand, the linear term (dashed–dotted line) is ascribed to the gradual closure of stiff pores (including intermediate pores). However, at pressures up to 500 MPa [see Figs 7(a) and (b), a zoom-in plot of Figs 6(a) and (b)], the dry moduli also show an exponential increase resulting from the closure of intermediate pores, similar to the behaviour of compliant pores at low pressures (<20 MPa). This behaviour at higher pressures has been documented by the ultrasonic measurements of several eclogites and country rocks under confining pressure up to 800 MPa by Wang *et al.* (2005), which exhibit an approximately exponential increase of the dry moduli with the increasing confining pressures.

We then substitute the parameters from Table 3 into our model and give the model predictions, as shown in Figs 8(a) and (b). First, we see that the C&S model (solid diamonds) gives much lower prediction of the solid-octadecane-saturated moduli in comparison with the experimental data (solid squares). The dual-porosity model (solid triangles) performs much better, but still has a clear discrepancy compared against the experimental data. Compared with the C&S model and the dual-porosity model, the present model (open triangles) gives more accurate estimates, which agree well with the laboratory measurements of the elastic moduli of the sandstone saturated with solid octadecane. Moreover, in the case of liquid octadecane in the pore space (open diamonds), the present model (solid circles) gives predictions that are consistent with the Gassmann theory.

4 DISCUSSION

One important feature of our scheme is that we assume the rock contains three types of pores, compliant, intermediate and stiff. Each type of pores is described to be spheroidal and has an aspect ratio. While this is a crude simplification in regard to the realistic pore shapes, such treatment seems to provide a good fit to the pressure dependency of the dry moduli. In this sense, this approximation is reasonable and effective.

Different from the recognition of a binary pore structure, we add a newly defined pore type, intermediate, to explain the pressure effects on the dry moduli at much higher pressures. As defined, intermediate porosity decreases in an exponential law at intermediate pressures, say 200−1000 MPa. We do not claim that this behavior of the pores at such high pressures is realistic. Indeed, those pressures are beyond the capacity of most rock physics laboratories and can even crush typical sandstone samples (Zhang *et al.* 1990; Wong *et al.* 1997; Fortin *et al.* 2007), though not mantle rocks (Wang *et al.* 2005). Sandstones at such pressures probably lie outside of the elastic regime. Yet the assumption of the behavior of velocities at such pressures is helpful for understanding of pore space geometry.

Application of our model requires the asymptotic values of the dry moduli in high-pressure limit that are usually unknown or hard to obtain directly from ultrasonic measurements due to the restriction of narrow measurement range of pressures. This work introduced pore-scale numerical simulations based on FEM in conjunction with the SCA to determine the effective aspect ratio of stiff pores and then compute the values by substituting the aspect ratio into the SCA. Such treatment implies that the numerical simulation results only correspond to the effects of stiff pores, while soft (compliant and intermediate) pores in the digital rock images are not resolved. While this assumption is reasonable for digital rock images with the voxel size of about 2−5 μm, the smallest voxel size currently available, future developments might provide more direct ways to characterize the pore shapes.

Another potential limitation of our approach is that the model is only suitable for pure sandstone. For shaley sandstone or other complex composite rocks, the pressure effects on the dry moduli are more complicated, and not only controlled by the closure of cracks. Moreover, the pore shapes information extracted from digital rock images is different from those of pure sandstone. Such influence might be studied in future work.

5 CONCLUSIONS

We present a simple scheme for fluid or solid substitution constrained by pore-scale numerical simulation based on finite element method. This scheme relates the change of the effective elastic moduli of porous and fractured rocks to the moduli of pore fill, including fluids, high-viscosity fluids and elastic solids. Pore-scale numerical simulations based on FEM are used to successfully determine the aspect ratio of stiff pores directly from microtomographic images in conjunction with the self-consistent medium theory. Then, the asymptotic values of dry moduli in high-pressure limit where only non-closable pores remain open are obtained using the SCA and then substituted into the scheme to estimate the effective elastic moduli of porous and fractured rocks saturated with various pore fills. The workflow avoids the need to assume the specific geometry of stiff pores and reduces the uncertainty of model predictions without any adjustable parameters. This strengthens the predictive power and usefulness of the model in predicting the effective elastic moduli of rocks resulting from the change in the moduli of pore fill. Successful application to a liquid- and solid-octadecane-saturated Bentheim sandstone has verified the accuracy and applicability of this scheme and indicated its potential in further exploitation and characterization of heavy oil and similar reservoirs.

ACKNOWLEDGEMENTS

We thank the financial support from the Curtin Reservoir Geophysics Consortium (CRGC) and the China Scholarship Council (CSC). This work was accomplished with the assistance of the Computational Infrastructure (NCI), which is supported by the Australian Government and the Pawsey Supercomputing Centre with funding from the Australian Government and the Government of Western Australia.

REFERENCES

Adam, L. & Otheim, T., 2013. Elastic laboratory measurements and modeling of saturated basalts, *J. geophys. Res.,* **118,** 840–851.

Adelinet, M., Fortin, J., Guéguen, Y., Schubnel, A. & Geoffroy, L., 2010. Frequency and fluid effects on elastic properties of basalt: experimental investigations, *Geophys. Res. Lett.,* **37,** doi:10.1029/2009GL041660.

Andrä, H. *et al.*, 2013. Digital rock physics benchmarks—Part II: computing effective properties, *Comput. Geosci.,* **50,** 33–43.

Arns, C.H., Knackstedt, M.A. & Mecke, K., 2003. Reconstructing complex materials via effective grain shapes, *Phys. Rev. Lett.,* **91,** 215506.

Arns, C.H., Knackstedt, M.A., Pinczewski, M.V. & Lindquist, W., 2001. Accurate estimation of transport properties from microtomographic images, *Geophys. Res. Lett.,* **28,** 3361–3364.

Arns, C.H., Knackstedt, M.A., Pinczewski, W.V. & Garboczi, E.J., 2002. Computation of linear elastic properties from microtomographic images: methodology and agreement between theory and experiment, *Geophysics,* **67,** 1396–1405.

Arns, C.H., Madadi, M., Sheppard, A.P. & Knackstedt, M.A., 2007. Linear elastic properties of granular rocks derived from X-ray-CT images, in *SEG Technical Program Expanded Abstracts 2007,* pp. 1711–1715, Society of Exploration Geophysicists.

Berryman, J.G., 1980. Long-wavelength propagation in composite elastic media II. Ellipsoidal inclusions, *J. acoust. Soc. Am.,* **68,** 1820–1831.

Berryman, J.G., 1999. Origin of Gassmann's equations, *Geophysics,* **64,** 1627–1629.

Ciz, R. & Shapiro, S.A., 2007. Generalization of Gassmann equations for porous media saturated with a solid material, *Geophysics,* **72,** A75–A79.

Cleary, M.P., Lee, S.-M. & Chen, I.-W., 1980. Self-consistent techniques for heterogeneous media, *J. Eng. Mech. Div.,* **106,** 861–887.

de Paula, O.B., Pervukhina, M., Makarynska, D. & Gurevich, B., 2012. Modeling squirt dispersion and attenuation in fluid-saturated rocks using pressure dependency of dry ultrasonic velocities, *Geophysics,* **77,** WA157–WA168.

Dubelaar, C.W. & Nijland, T.G., 2015. The Bentheim Sandstone: geology, petrophysics, varieties and its use as dimension stone, in *Engineering Geology for Society and Territory,* **Vol. 8,** pp. 557–563, Springer.

Fortin, J., Guéguen, Y. & Schubnel, A., 2007. Effects of pore collapse and grain crushing on ultrasonic velocities and Vp/Vs, *J. geophys. Res.,* **112,** doi:10.1029/2005JB004005.

Gassmann, F., 1951. Über die Elastizität poröser Medien: Vierteljahrsschrift der Naturforschenden Gesellschaft in Zürich, **96,** 1–23.

Glubokovskikh, S., Gurevich, B. & Saxena, N., 2016. A dual-porosity scheme for fluid/solid substitution, *Geophys. Prospect.,* **64,** 1112–1121.

Kuster, G.T. & Toksöz, M.N., 1974. Velocity and attenuation of seismic waves in two-phase media: Part I. Theoretical formulations, *Geophysics,* **39,** 587–606.

Leurer, K.C. & Dvorkin, J., 2006. Viscoelasticity of precompacted unconsolidated sand with viscous cement, *Geophysics,* **71,** T31–T40.

Liu, X., Yin, X. & Luan, X., 2018. Seismic rock physical modelling for gas hydrate-bearing sediments, *Sci. China Earth Sci.,* **61,** 1261–1278.

Makarynska, D., Gurevich, B., Behura, J. & Batzle, M., 2010. Fluid substitution in rocks saturated with viscoelastic fluids, *Geophysics,* **75,** E115–E122.

Mavko, G. & Saxena, N., 2013. Embedded-bound method for estimating the change in bulk modulus under either fluid or solid substitution, *Geophysics,* doi:10.1190/geo2013-0074.1.

Norris, A., 1985. A differential scheme for the effective moduli of composites, *Mech. Mater.,* **4,** 1–16.

Ogushwitz, P., 1985. Applicability of the Biot theory. I. Low-porosity materials, *J. acoust. Soc. Am.,* **77,** 429–440.

Ollion, J., Cochennec, J., Loll, F., Escudé, C. & Boudier, T., 2013. TANGO: a generic tool for high-throughput 3D image analysis for studying nuclear organization, *Bioinformatics,* **29,** 1840–1841.

Roberts, A.P. & Garboczi, E.J., 2000. Elastic properties of model porous ceramics, *J. Am. Ceram. Soc.,* **83,** 3041–3048.

Saenger, E.H., Lebedev, M., Uribe, D., Osorno, M., Vialle, S., Duda, M., Iglauer, S. & Steeb, H., 2016. Analysis of high-resolution X-ray computed tomography images of Bentheim sandstone under elevated confining pressures, *Geophys. Prospect.,* **64,** 848–859.

Saxena, N. & Mavko, G., 2014. Exact equations for fluid and solid substitution, *Geophysics,* **79** (3), doi:10.1190/geo2013-0187.1.

Saxena, N. & Mavko, G., 2015. Effects of fluid-shear resistance and squirt flow on velocity dispersion in rocks, *Geophysics,* **80**(2), doi:10.1190/geo2014-0304.1.

Saxena, N., Mavko, G., Hofmann, R., Gurevich, B., Glubokovskikh, S., Aliyeva, S. & Dutta, P., 2016. Rock-physics models for heavy-oil and organic-solid substitution, *Leading Edge,* **35,** 506–510.

Shapiro, S.A., 2003. Elastic piezosensitivity of porous and fractured rocks, *Geophysics,* **68,** 482–486.

Smith, T.M., Sondergeld, C.H. & Rai, C.S., 2003. Gassmann fluid substitutions: a tutorial, *Geophysics,* **68,** 430–440.

Sun, Y., Gurevich, B., Lebedev, M., Glubokovskikh, S., Mikhaltsevitch, V. & Guo, J., 2018. A triple porosity scheme for fluid/solid substitution: theory and experiment, *Geophys. Prospect.,* 1–12.

Tsai, H.-C. & Lee, C.-C., 1998. Compressive stiffness of elastic layers bonded between rigid plates, *Int. J. Solids Struct.,* **35,** 3053–3069.

Vernik, L., 1998. Acoustic velocity and porosity systematics in siliciclastics, *Log Analyst,* **39** (4), 27–35.

Walsh, J., 1965. The effect of cracks on the compressibility of rock, *J. geophys. Res.,* **70,** 381–389.

Wang, Q., Ji, S., Salisbury, M.H., Xia, B., Pan, M. & Xu, Z., 2005. Pressure dependence and anisotropy of P-wave velocities in ultrahigh-pressure metamorphic rocks from the Dabie–Sulu orogenic belt (China): implications for seismic properties of subducted slabs and origin of mantle reflections, *Tectonophysics,* **398,** 67–99.

Wong, T., David, C. & Zhu, W., 1997. The transition from brittle faulting to cataclastic flow in porous sandstones: mechanical deformation, *J. geophys. Res.,* **102,** 3009–3025.

Zhang, J., Wong, T.F. & Davis, D.M., 1990. Micromechanics of pressure-induced grain crushing in porous rocks, *J. geophys. Res.,* **95,** 341–352.

Zimmerman, R.W., 1991. *Compressibility of Sandstones,* Vol. **29,** Elsevier.

Zimmerman, R.W., Somerton, W.H. & King, M.S., 1986. Compressibility of porous rocks, *J. geophys. Res.,* **91,** 12 765–12 777.